



# Transition metal atom–doped monolayer MoS<sub>2</sub> in a proton-exchange membrane electrolyzer

J. Mo <sup>a, d</sup>, S. Wu <sup>a, d</sup>, T.H.M. Lau <sup>a</sup>, R. Kato <sup>b</sup>, K. Suenaga <sup>b</sup>, T.-S. Wu <sup>c</sup>, Y.-L. Soo <sup>c</sup>, J.S. Foord <sup>a</sup>, S.C.E. Tsang <sup>a, \*</sup>

<sup>a</sup> The Wolfson Catalysis Centre, Department of Chemistry, University of Oxford, Oxford, OX1 3QR, UK

<sup>b</sup> National Institute of Advanced Industrial Science and Technology (AIST), Central 5, 1-1-1 Higashi, Tsukuba, Ibaraki 305-8565, Japan

<sup>c</sup> Department of Physics, National Tsing Hua University, Hsinchu, Taiwan

## ARTICLE INFO

### Article history:

Received 14 August 2019

Received in revised form

18 September 2019

Accepted 25 September 2019

Available online 7 February 2020

### Keywords:

Electrolyzer

Hydrogen

Water electrolysis

Catalysts

Non-noble metal

Monolayer MoS<sub>2</sub>

## ABSTRACT

There has been a substantial research effort worldwide to develop non-noble metal catalysts for H<sub>2</sub> production from water splitting using renewable energy sources, but most data were evaluated by voltammetry in laboratories. Here, exposed basal planes of MoS<sub>2</sub> monolayer nanosheets with metal dopants across the first transition metal (TM) series in the periodic table (Fe, Co, Ni, Cu) are used as cathode catalysts for the proton-exchange membrane (PEM) water splitting in an electrolyzer under typical conditions of strong acidity with more negative applied voltage. Extended X-ray absorption fine structure spectroscopy (EXAFS) analysis and high-angle annular dark-field scanning transmission electron microscopy (HAADF–STEM) images show a direct proof on the single TM atoms residing at the surface basal sites, which subtly modify the electrocatalytic activity of the monolayer MoS<sub>2</sub>, depending on their electronic and metal-hydrogen binding ability. We report that Co–<sup>s</sup>MoS<sub>2</sub> yields the highest current density in an electrolyzer with the hydrogen evolution reaction (HER) activity comparable with that of the commercial 20 wt% Pt/C under industrial applicable conditions. A general trend for the other TMs has also been established as evidenced by the change in TM effective nuclear charge across the periodic table, which perturbed the TM–Mo interaction and hence affects the HER activity.

© 2019 Published by Elsevier Ltd. This is an open access article under the CC BY-NC-ND license (<http://creativecommons.org/licenses/by-nc-nd/4.0/>).

## 1. Introduction

Global CO<sub>2</sub> emissions generated from fossil fuel sources have reached a 2.7% growth this year, the highest since the last decade [1]. As a result, in hopes of decarbonizing the global economy to tackle against the strikingly high atmospheric green house gas concentrations, fossil fuel usage has to be reduced to limit the emission of pollutants and protect the environment [2]. Hydrogen energy appears to be a promising renewable energy source to retard the heavy dependence on fossil fuels with its sustainability and environmental impact of modern-day energy consumption [3,4]. The use of catalytic water splitting with a proton-exchange membrane (PEM) electrolyzer provides a spectacular concept to convert renewable electrical energy into storable and transportable hydrogen energy [5]. The hydrogen evolution reaction (HER),

$2\text{H}^+ + 2\text{e}^- \rightarrow \text{H}_2$ , is a fundamental step of water splitting in an electrolyzer system. Achieving high energetic efficiency for water splitting requires the use of a catalyst to minimize the overpotential necessary to drive the HER [6].

The platinum-based noble metal materials are widely used in industry for electrochemical HER because of its intrinsic electrocatalytic activity and stability [7,8]. However, the high material cost and scarcity of Pt-based electrocatalysts have refrained it from being used widely in the electrolyzer. Therefore, exploiting earth-abundant yet high-efficiency transition metal (TM) based materials for the electrolytic hydrogen production reaction (HER) is of paramount importance. Commercially available molybdenum disulfide (MoS<sub>2</sub>) with a layered structure has recently drawn extensive research attention for the HER electrocatalysts because of its specific electrochemical catalytic properties and high stability in acidic environment [9–12].

It is generally accepted that the trigonal prismatic coordinated Mo phase, namely the 2H phase, is the most stable form of MoS<sub>2</sub> [13]. It can be easily obtained from nature and is therefore widely used catalytically. Briefly, an MoS<sub>2</sub> layer is composed of a

\* Corresponding author.

E-mail address: [edman.tsang@univ.ox.ac.uk](mailto:edman.tsang@univ.ox.ac.uk) (S.C.E. Tsang).

<sup>d</sup> Co-first author.

hexagonally arranged molybdenum plane that is covalently bonded between 2 hexagonal sulfur planes in the proximity, while weaker van der Waals force dominantly holds the interlayers. As a result, it is possible to enhance the electron hopping process across the van der Waals gaps by reducing the number of layers of MoS<sub>2</sub>, thereby facilitating the charge transfer kinetics on the surface [14,15]. Regarding the active sites, Mo edges (10<sup>-10</sup>) and the S edges (<sup>-</sup>1010) of the pristine form of MoS<sub>2</sub> provide two dominant sites for electrochemical hydrogen evolution process, whereas the pristine basal planes (0001) are typically electrochemically inactive to the overall HER catalytic activity [16,17]. To generate more active sites, it is essential to activate the basal plane for enhancing the MoS<sub>2</sub> catalytic ability. A general strategy is to introduce TM species to the separated monolayer basal planes, namely the dopant method [18], which can strengthen the binding energy of hydrogen on the active sites. In addition, the relatively larger quantity of basal sites in comparison with edge sites in a good-quality monolayer <sup>s</sup>MoS<sub>2</sub> sample (Fig. S1) would reflect the TM modification on the basal sites. For instance, we have previously reported that by anchoring single Co atoms tetrahedrally to the sulfur sites of the monolayer basal plane, the neighboring S sites on the surface can be enhanced through a Co–S interaction. This could in turn attenuate the Gibbs free energy of hydrogen adsorption toward a maximum thermodynamic enthalpy value, resulting in an increase of HER rate compared with an undoped monolayer in cyclic voltammetry [19].

Herein, we expand our scope by exploring an array of TM dopants and investigate the way they interact with the basal plane of monolayer MoS<sub>2</sub>. More importantly, we have used the TM-modified MoS<sub>2</sub> in an industrial electrolyzer via the proton-exchange membrane setup (Fig. 1). By using the state-of-the-art scanning transmission electron microscopy coupled with high-angle annular dark-field imaging techniques in conjunction with ultrafast X-ray absorption spectroscopy, all the TM dopants are observed to be singly anchored to the surface basal plane without formation of any metal clusters, among which Co-<sup>s</sup>MoS<sub>2</sub> is found to exhibit the highest current density in the HER inside the electrolyzer across the four M-<sup>s</sup>MoS<sub>2</sub> with comparable performance as the 20 wt% Pt/C commercial catalysts.

## 2. Experimental section

### 2.1. Preparation of single-layered MoS<sub>2</sub> (<sup>s</sup>MoS<sub>2</sub>)

The single-layered MoS<sub>2</sub> (<sup>s</sup>MoS<sub>2</sub>) was synthesized by chemical exfoliation of bulk commercially available MoS<sub>2</sub> using BuLi intercalation [19,20].

#### 2.1.1. Single-layered MoS<sub>2</sub> (<sup>s</sup>MoS<sub>2</sub>) synthesis

Bulk MoS<sub>2</sub> powder (2 g) was soaked in 1.6 M n-butyllithium/hexane (16 mL) under nitrogen atmosphere for 48 h. After intercalation by lithium, solid Li<sub>x</sub>MoS<sub>2</sub> was isolated by vacuum filtration, followed by washing with hexane to remove the excess n-butyllithium. It was then dried in a vacuum oven (70 °C) for 24 h. The dried product was then immersed into 500 mL of deionized water. The solution was placed in the sonication bath for 12 h to assist the completion of exfoliation and then centrifuged at 5000 r.p.m. for 15 min. The supernatant collected was filtered using vacuum filtration, followed by washing with water. The exfoliated product was dried under vacuum for 24 h.

#### 2.2. Synthesis of single TM atom-doped <sup>s</sup>MoS<sub>2</sub>

The single TM atom (Fe, Ni, Co, Cu)-doped <sup>s</sup>MoS<sub>2</sub> catalysts were prepared by hydrothermal method. Each metal (II) acetate precursor (0.2 mmol) (except Co(III) acetate) was added to 1 mL of 0.5 mM thiourea solution and left overnight to form the corresponding metal-thiourea complex. The complex solution was added to 30 mL of the <sup>s</sup>MoS<sub>2</sub> suspension prepared by dispersing 30 mg of <sup>s</sup>MoS<sub>2</sub> in 30 mL of isopropanol/water (3:1, v/v) together with 15 μL of 5 wt% Nafion® 117 solution (stabilizer). The resulting homogenous solution was transferred into an autoclave, followed by hydrothermal treatment at 160 °C for 24 h. The precipitate was then filtered by vacuum filtration, washed with deionized water, and dried under vacuum for 12 h to obtain the final catalyst powder [19].

#### 2.3. Materials characterizations

The scanning transition electron microscopy–electron energy loss spectroscopy (STEM-EELS) was performed using a JEOL 2100F TEM with a DELTA aberration corrector operated at 60 kV and a GIF Quantum for spectroscopy. For the X-ray absorption spectroscopy (XAS), dopant metal (Fe, Co, Ni, Cu) K-edge X-ray absorption spectrum was conducted in fluorescence mode at the BL07A XAS beamline at the National Synchrotron Radiation Center, Taiwan.

#### 2.4. Electrochemical measurement

##### 2.4.1. Linear sweep voltammetry measurement

A three-electrode system monitored by μ-AUTOLAB III potentiostat (Eco-Chemie, the Netherlands) was applied to carry out all the LSV measurements. A platinum coil was used as the counter electrode, and Ag/AgCl (1 mol L<sup>-1</sup> KCl) was used as the reference electrode in this study. To prepare the catalyst ink for the working electrode, 4 mg of the electrocatalyst and 80 μL of 5 wt% Nafion® 117 solution is dispersed in 1 mL of water/ethanol (4:1 v/v) and then followed by 30-min sonication. The homogeneous catalyst ink was then drop-casted onto the surface of a glassy carbon electrode with a surface diameter of 3 mm. All measurements were calibrated with respect to the reversible hydrogen electrode (RHE)(Fig. S2).

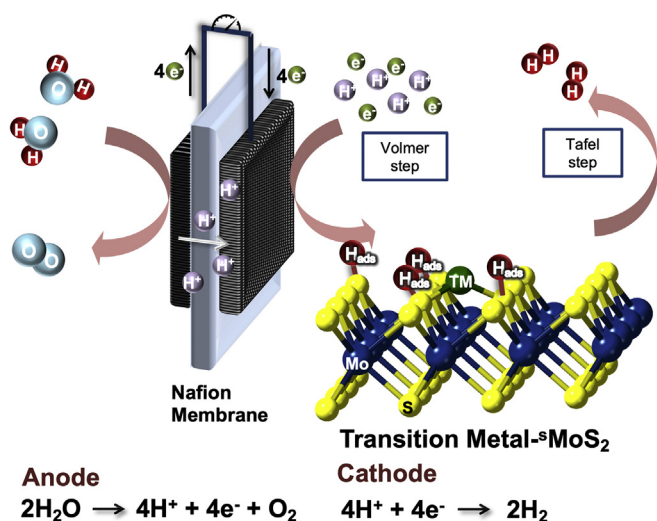


**Fig. 1.** A schematic overview of a PEM electrolyzer where the anode activates H<sub>2</sub>O to O<sub>2</sub> with H<sup>+</sup> diffusing across the Nafion membrane under potential to a cathodic metal catalyst for H<sub>2</sub> production. PEM, proton-exchange membrane.

#### 2.4.2. Membrane electrode assembly fabrication and electrolyzer testing

The electrolysis cell testing in a single PEM electrolyzer with a  $1.5 \times 1.5 \text{ cm}^2$  geometric surface area was carried out by one-pass feed of the anode with deionized (DI) water at a flow rate of 4 mL/min. The electrolyzer was operated at 80 °C and under ambient pressure for all measurements. The polarization curves were recorded using a TENMA programmable potentiostat. The rate of hydrogen produced can be derived through the measurement of current density.

Membrane electrode assemblies (MEAs) were fabricated using the Nafion 115 membrane placed in between the two catalyst electrodes. The Nafion 115 membranes were first cut into  $2.5 \times 2.5 \text{ cm}^2$  pieces and then pretreated by soaking in 3%  $\text{H}_2\text{O}_2$ , 0.5 M  $\text{H}_2\text{SO}_4$ , and Millipore water for an hour at 80 °C. After that, the single TM atom (Fe, Ni, Co, Cu)-doped  $^5\text{MoS}_2$  catalysts and Nafion ionomer (5 wt% solution) were mixed in a 3:1 wt ratio. Separately, the  $\text{IrO}_2$  catalyst and Nafion ionomer (5 wt% solution) were also mixed in a 3:1 wt ratio. The single TM atom (Fe, Ni, Co, Cu)-doped  $^5\text{MoS}_2$  and  $\text{IrO}_2$  catalyst/ionomer mixtures were both dispersed in 3:1 vol ratio mixture of isopropanol and DI water. The catalyst/ionomer solutions were sonicated for 1 h and then deposited on the opposite sides of the Nafion membrane by spray casting. Catalyst ink of the commercial 20 wt% Pt/C, which was to be used as the reference, was also prepared via the same method as that of metal-doped  $\text{MoS}_2$ . The single TM atom (Fe, Ni, Co, Cu)-doped  $^5\text{MoS}_2$  and 20 wt% Pt/C were loaded on the cathode side at  $4.5 \pm 0.25 \text{ mg cm}^{-2}$ , and  $\text{IrO}_2$  catalysts were loaded on the anode side at  $2.5 \pm 0.2 \text{ mg cm}^{-2}$  over a  $1.5 \times 1.5 \text{ cm}^2$  active area. The catalyst-loaded Nafion membrane was hot-pressed between carbon paper at the cathode side and Ti mesh at the anode side at 135 °C.

### 3. Results and discussions

The single-layer molybdenum disulfide ( $^5\text{MoS}_2$ ) was synthesized by the lithium intercalation of commercial bulk molybdenum disulfide precursor [19]. Four TMs, Fe, Co, Ni, and Cu, of the same period were chosen to be the dopant on  $^5\text{MoS}_2$  via the hydrothermal doping method.

#### 3.1. Structural characterization of single TM atom-doped $^5\text{MoS}_2$

The coordination environment of the TM-doped  $^5\text{MoS}_2$  was first probed by extended X-ray absorption fine structure spectroscopy (EXAFS). Figs. S3–6 shows the  $k^2$ -weighted Fourier transformed R-space spectra for the Fe, Co, Ni, and Cu K-edge of the metal-doped  $^5\text{MoS}_2$ . Parameters obtained from the least-square fittings are displayed in Figs. S3–6. First shell peak fitting from the EXAFS results have shown that the TMs are bonded to sulfur atoms in trigonal prismatic, tetrahedral, or octahedral manner, while first shell metal-metal interaction is not observed. This suggests that the metal atoms are not in a cluster state but in a singly anchored form on the surface S sites of the basal plane. Meanwhile wavelet restoration (WR) on the chi-functions of the metal-doped  $^5\text{MoS}_2$  was also performed. This serves as a powerful tool to distinguish contributions between light and heavy elements because it provides sharp resolution in  $k$  space and  $R$  space. In fact, as shown in Fig. 2 (a)–(d), all the WR contour plots show only one energy maxima at  $4\text{--}6 \text{ \AA}^{-1}$ , which matches well with the chi-function of the TM-S scattering path as calculated in the least-square fitting (Fig. 2 (e)–(h)). In addition, no energy maximum at higher wave-number can be detected when compared with the metal foils in Fig. S7. This further confirms that the TMs are atomically anchored to the surface S sites. Looking at the individual TM-doped samples, it is interesting to observe that Co is bonded tetrahedrally, whereas

its neighbors, for instance, Fe and Ni, are bonded octahedrally to neighboring surface S atoms and S atoms from thiourea. Meanwhile, Cu is bonded in a trigonal prismatic manner to 3 surface S atoms. This can be explained by the general ligand field stabilization where the actual oxidation state is important in determining the number of ligands attached. Bearing a  $d^7$  configuration and a high oxidation state of Co(III) used, the smaller size of Co(III) with respect to bulkier S renders the Co- $^5\text{MoS}_2$  in a tetrahedrally bonded form, whereas other M(II) complexes are bonded more favorably in the octahedral state with higher ligand stabilization. This is also evidenced by the sharp white line intensity in Fig. 2 (j) which implies a strong electronic transition. In contrast, owing to larger size and lower oxidation state of Fe (II) and Ni (II) used, they are bonded octahedrally (Fig. 2(i) and Fig. 2(k)). Furthermore, the intriguing fact that Cu, despite having the smallest size, is 3-coordinated presumably owing to the distortion from tetrahedral where non-surface S coordination is much weakened or lengthened as suggested by the absence of the pre-edge peak in X-ray absorption near edge spectroscopy (XANES) (Fig. S8).

To visualize the spatial position of the TM dopants across the same period (Fe, Co, Ni, Cu), which show different electrocatalytic properties on the basal plane of  $^5\text{MoS}_2$ , high-angle annular dark-field (HAADF) imaging combined with electron energy loss spectroscopy (EELS) mapping of M- $^5\text{MoS}_2$  were performed by high-resolution scanning transmission electron microscopy (HR-STEM) (Fig. 3 and Figs. S9–10) and simulation (Fig. S11). The STEM analyses of the M- $^5\text{MoS}_2$  show a characteristic and well-ordered hexagonal pattern of the honey comb-like structure which corresponds to the monolayer  $^5\text{MoS}_2$  [13]. Owing to the Z contrast nature of annular dark-field (ADF) imaging, Mo atoms (blue, Fig. 3(a)) would appear to be brighter than S atoms (yellow, Fig. 3(a)). From Fig. 3(a), a very bright spot can be clearly observed on top of the Mo position sandwiched by S atoms. This is attributed to the single Co atom sitting on top of the trigonal prismatic Mo atom (Mo atop site) [20]. To further confirm the presence of a Co atom in these bright contrast spots, simultaneous HAADF and EELS acquisitions were performed. A line scan for both HAADF intensity and EELS was taken across a bright contrast spot, indicated in Fig. 3(a), yielding an HAADF intensity profile (Fig. 3(b)). Moreover, Fig. 3(c) depicts EELS extracted across a line containing the single Co metal dopants on the Mo atop site, indicated by colored cycles in Fig. 3 (a). These spectra demonstrate the presence of a Co atom in the atomic column (blue profile), with the signature  $L_3$  and  $L_2$  edges occurring at the expected energy levels. Such features are not present in the EELS of the positions before (green profile) and after (yellow profile) the atomic site. In addition, similar STEM characteristic properties were also observed in the Ni and Fe- $^5\text{MoS}_2$  as in the supporting information (Figs. S9–10). The images provide the direct microscopy evidence of doping single TM atoms onto the basal plane of the synthesized monolayer  $\text{MoS}_2$  in a position of the Mo atop sites.

#### 3.2. Electrochemical performance

The data clearly suggest that the choice of the TM dopant greatly influences the coordination environment and hence the intrinsic surface properties of the basal plane of the  $\text{MoS}_2$ . Meanwhile, it is generally accepted that the interaction of the metal dopant with the surface edge S sites and Mo sites can influence the H adsorption enthalpy in HER [21]. It would be exciting to probe the correlation between TM doping and basal plane modification and see how it would affect the HER.

The electrocatalytic HER performance of the single TM atom-doped  $^5\text{MoS}_2$  (TM- $^5\text{MoS}_2$ ) catalysts and commercial 20 wt% Pt/C reference was explored using both linear sweep voltammetry (LSV)



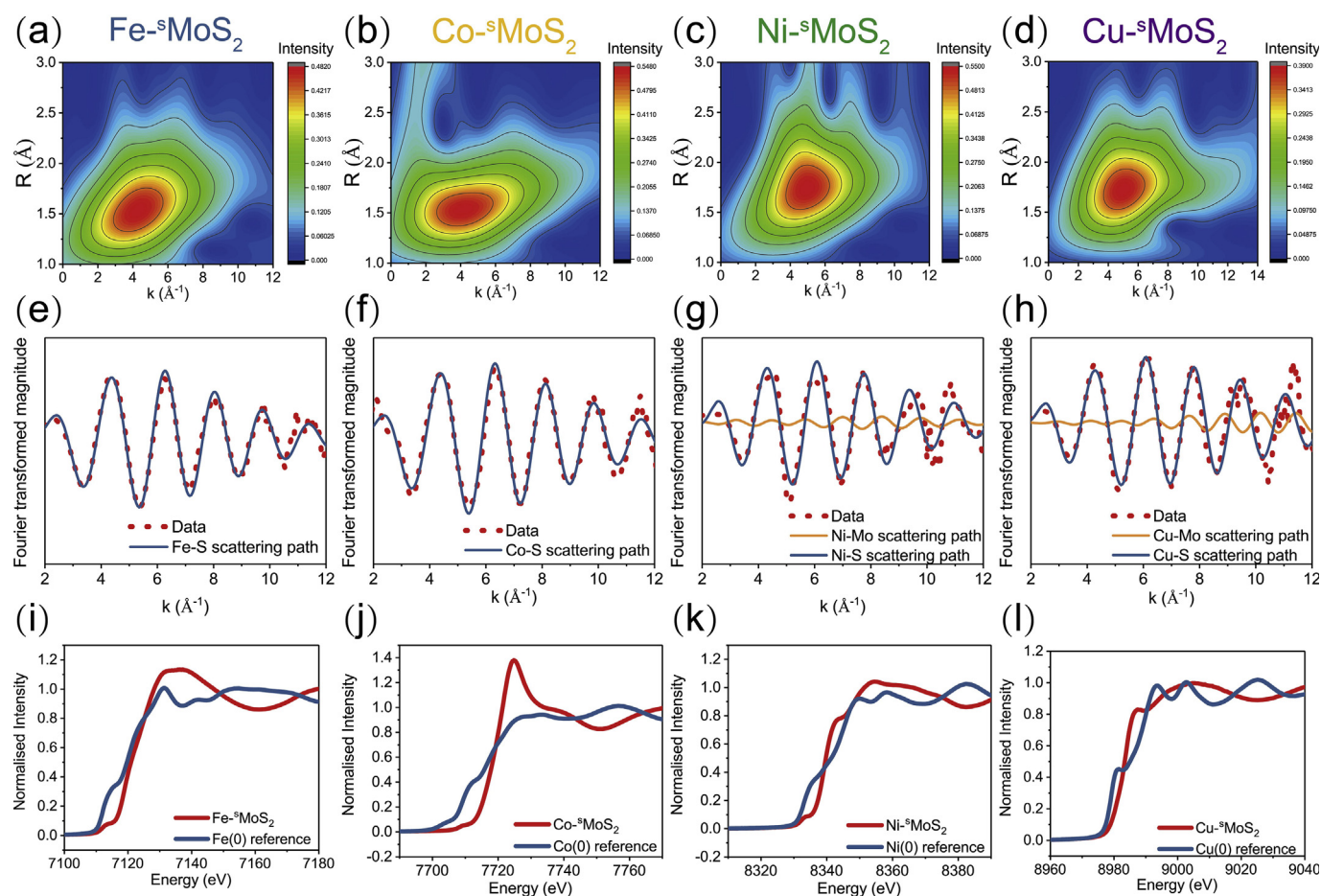


**Fig. 2.** EXAFS analysis of single TM atom-doped  $5\text{MoS}_2$ . (a)–(d) Wavelet restoration using Morlet wavelet; (e)–(h) Fourier transformed chi-function and scattering paths used in the first shell and second shell least-square fitting for Fe- $5\text{MoS}_2$ , Co- $5\text{MoS}_2$ , Ni- $5\text{MoS}_2$ , and Cu- $5\text{MoS}_2$ , respectively; (i)–(l) XANES spectra of Fe- $5\text{MoS}_2$ , Co- $5\text{MoS}_2$ , Ni- $5\text{MoS}_2$ , and Cu- $5\text{MoS}_2$  compared with corresponding metal (0) foils. EXAFS, extended X-ray absorption fine structure spectroscopy; XANES, X-ray absorption near edge spectroscopy.

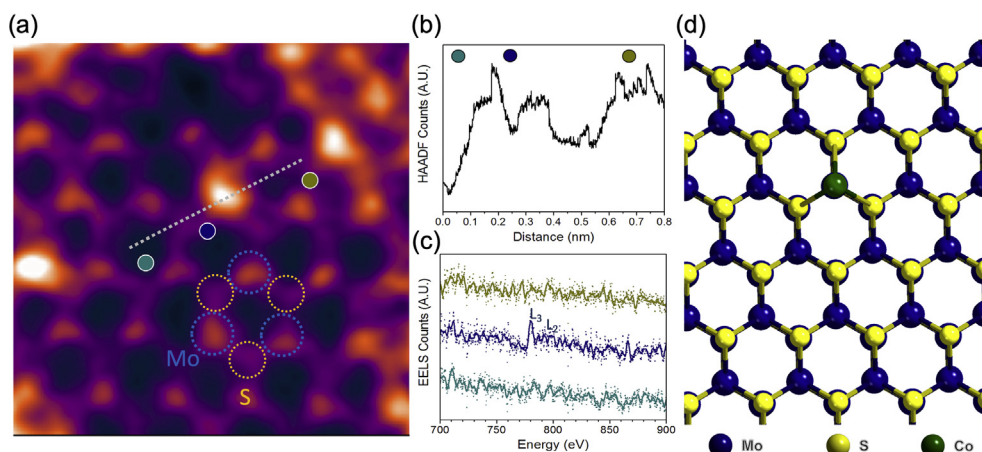


**Fig. 3.** Detailed atomic resolution HAADF-STEM characterization of the basal plane of used Co- $5\text{MoS}_2$ . (a) HAADF-STEM images of Co- $5\text{MoS}_2$ . (b) ADF and (c) EELS acquired along the line in (a). (d) Co at the Mo atop site model corresponding to (a). HAADF-STEM, high-angle annular dark-field scanning transmission electron microscopy; EELS, electron energy loss spectroscopy. ADF, annular dark-field.

and a PEM electrolyzer with reference to industrial applicable reaction conditions. At the outset of this study, four different metal-doped  $5\text{MoS}_2$  (Fe, Co, Ni, Cu) were used as the cathode catalyst in the electrochemical testing. Fig. 4(a) shows the HER polarization curves of the different TM doping  $\text{MoS}_2$  cathode catalysts and the

reference 20 wt% Pt/C. Clearly, the catalytic performance followed the trend of  $\text{Cu-}5\text{MoS}_2 < \text{Fe-}5\text{MoS}_2 < 5\text{MoS}_2 < \text{Ni-}5\text{MoS}_2 < \text{Co-}5\text{MoS}_2 < 20 \text{ wt\% Pt/C}$  at an applied potential of  $-1.0 \text{ V}$  to  $-1.8 \text{ V}$ . The activity ranking order resembles their onset potentials evaluated in the LSV in Fig. 4(c). It is interesting to note that the catalytic

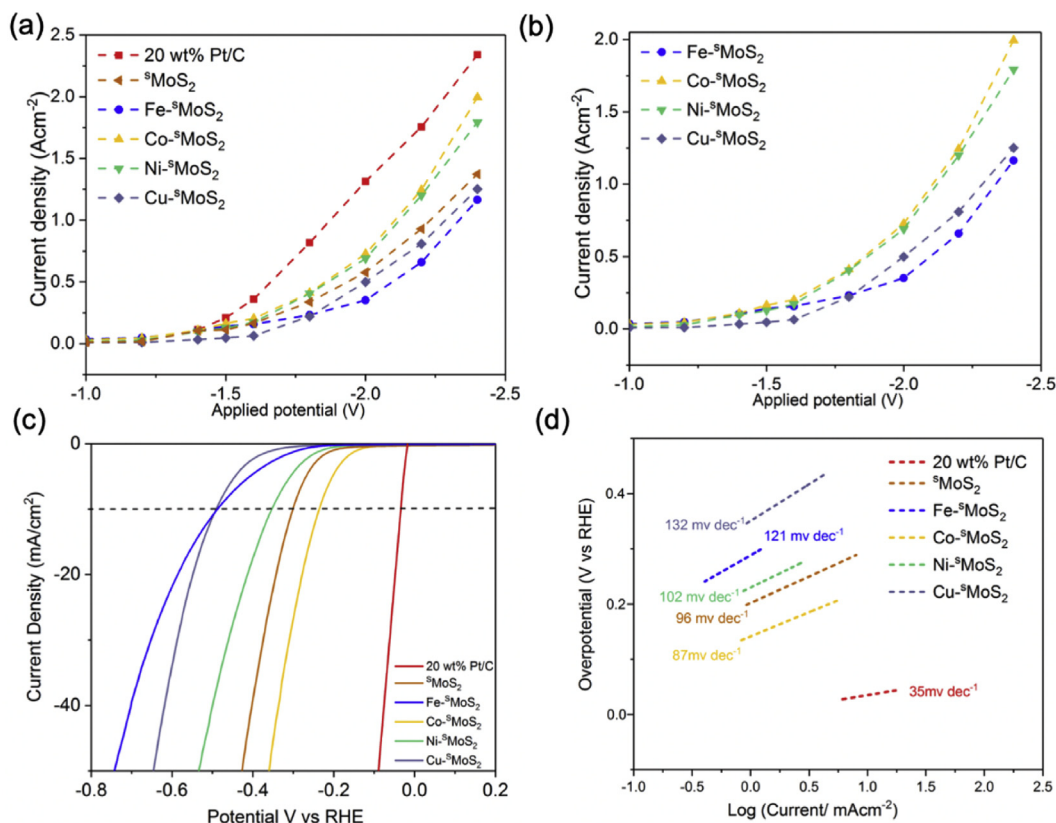


**Fig. 4.** Electrochemical performance of transition metal-doped single-layer MoS<sub>2</sub>. (a) and (b) Current-voltage polarization curves of the electrolyzer with different catalysts at T = 80 °C. The TM-MoS<sub>2</sub> or 20 wt% Pt/C reference was used as cathode catalyst, and the anode catalyst was IrO<sub>2</sub> for all MEAs. (c) Linear sweep voltammetry of the TM-MoS<sub>2</sub> and 20 wt% Pt/C at a scan rate of 2 mV/s in 0.5 M H<sub>2</sub>SO<sub>4</sub> electrolyte and their corresponding Tafel plot (d). MEA, membrane electrode assembly; RHE, reversible hydrogen electrode.

activity trend in Fig. 4(b) switched to Cu-MoS<sub>2</sub> > Fe-MoS<sub>2</sub> while applying more negative potential (−2.0 V to −2.4 V) in the electrolyzer device. The switch in activity order of this pair of TMs can also be reflected in Fig. 4(c) when higher overpotential beyond the onset potentials were used in LSV. According to Tafel plots shown in Fig. 4(d), the higher Tafel slopes ( $\geq 100$  mV dec<sup>−1</sup>) suggest that the surface-H bond formation (Volmer step) is likely to be rate determining at low potentials, and thus, the hydrogen adsorption energy on the metal surface should be the determining factor [19,22]. However, when used higher potentials and strong acidity (Nafion membrane is strongly acidic) in the real electrolyzer device, it will favor more toward Tafel H-H recombination step accounting the switch of the activity order of Cu-MoS<sub>2</sub> > Fe-MoS<sub>2</sub> (Cu-H is weaker than Fe-H). Nevertheless, Co-MoS<sub>2</sub> yields the highest current density in both LSV and electrolyzer among all the TMs studied.

There have been previous attempts to model activity by doping single TM atoms onto the basal MoS<sub>2</sub> [19]. Gibbs free energy of hydrogen adsorption ( $\Delta G_H$ ) is used as a descriptor for HER activity. It is believed  $\Delta G_H$  on a composite material plays an important role in electrochemical production of hydrogen gas: too weak H adsorption on the surface will not favor the electrochemical reaction and too strong H adsorption would also not facilitate H<sub>2</sub> recombination and desorption. Thus, this theoretical value should be as close as to 0 to maximize the overall thermodynamic enthalpy value for H surface adsorption, surface recombination, and desorption processes in HER. The appropriate downshift of the conduction band of the composite and the absence of Co-Mo bond (Co(III) tetrahedrally bonded with surface S does not allow the direct interaction with Mo geometrically to give Co-Mo) enable the

Gibbs free energy of hydrogen adsorption ( $\Delta G_H$ ) on S sites approaching to the zero value [23]. As for Fe, Ni, and Cu-MoS<sub>2</sub>, the TM-Mo bond in non-tetrahedral forms allows the electronic modification by the Mo site which have caused a greater deviation of  $\Delta G_H$  from zero. Furthermore, the trend that Ni > Cu > Fe can be interpreted from the XANES results. Linear combination fitting of the XANES spectra (Fig. 5 and Table 1) for Ni, Cu, and Fe reveals that the average oxidation state is +0.9, +1.2, and +2.0, respectively, owing to contribution of bonding electrons from S ligands. The greater nuclear charge of the metal seems to have rendered the further deviation of the conduction band of Mo, which in turn attenuates the hydrogen production ability.

It is imperatively important from this comparative study that the information on activity evaluation derived from LSV may not be the same as that in the real electrolyzer device. The use of the acidic Nafion membrane ( $\sim 0.1$  S cm<sup>−1</sup>) and higher applied voltage in the electrolyzer are markedly different from those conditions used in LSV. Under the electrolyzer conditions, the whole applied potential range of the commercially available 20 wt% Pt/C activity is still higher than that of all the other TM-MoS<sub>2</sub> catalysts with a current density of 2.34 A cm<sup>−2</sup> at −2.4 V. However, the Co-MoS<sub>2</sub> which exhibits the best performance among all the TM-doped MoS<sub>2</sub> in this study gives a current density of 2.00 A cm<sup>−2</sup> at the same applied potential which is only 14.5% lower than the commercial Pt catalyst, while it has to be pointed out that the Co metal loading in the Co-MoS<sub>2</sub> catalyst is only 3 wt% from inductively coupled plasma mass spectrometry (ICP-MS) analysis (Table S1) which is much lower than the 20 wt% Pt/C.

Fig. 4 (c) and (d) show the LSV of M-MoS<sub>2</sub> and 20 wt% Pt/C and corresponding Tafel slopes. Apart from the 20 wt% Pt/C, Co-MoS<sub>2</sub>

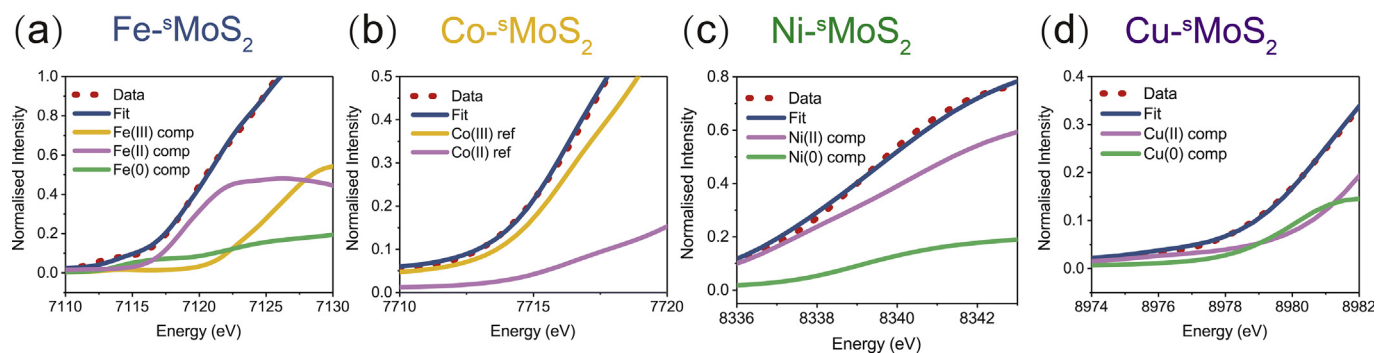


**Fig. 5.** Linear combination fitting of XANES spectra for (a) Fe-<sup>s</sup>MoS<sub>2</sub>, (b) Co-<sup>s</sup>MoS<sub>2</sub>, (c) Ni-<sup>s</sup>MoS<sub>2</sub>, and (d) Cu-<sup>s</sup>MoS<sub>2</sub>. XANES, X-ray absorption near edge spectroscopy.

**Table 1**  
Average oxidation state of TM-MoS<sub>2</sub> calculated from XANES spectra.

Fe		Co		Ni		Cu	
Component	Weight (%)	Component	Weight (%)	Component	Weight (%)	Component	Weight (%)
Fe(III)	40.7	Co(III)	80.2	Ni(II)	47.5	Cu(II)	61.7
Fe(II)	37.6	Co(II)	19.8	Ni(0)	52.5	Cu(0)	38.3
Fe(0)	21.7	/	/	/	/	/	/
Average O.S.	+2.0	Average O.S.	+2.8	Average O.S.	+0.9	Average O.S.	+1.2

TM, transition metal; XANES, X-ray absorption near edge spectroscopy.

significantly promoted the <sup>s</sup>MoS<sub>2</sub> showing the lowest onset potential of 230 mV at 100 mA cm<sup>-2</sup> among all the TM-<sup>s</sup>MoS<sub>2</sub> in this study, followed by <sup>s</sup>MoS<sub>2</sub> < Ni-<sup>s</sup>MoS<sub>2</sub> < Fe-<sup>s</sup>MoS<sub>2</sub> < Cu-<sup>s</sup>MoS<sub>2</sub>. The LSV is consistent to Fig. 4 (a) PEM electrolyzer performance in general, while the lower onset potential of <sup>s</sup>MoS<sub>2</sub> compared with Ni promoted <sup>s</sup>MoS<sub>2</sub> showing poorer catalytic performance in the PEM electrolyzer testing than Ni-<sup>s</sup>MoS<sub>2</sub> when higher potential was used. In addition, the current density of Cu-<sup>s</sup>MoS<sub>2</sub> overtakes the Fe-<sup>s</sup>MoS<sub>2</sub> after -0.5 V in LSV measurement which is consistent to the electrolyzer testing which overtaking is happening at -1.8 V.

Also, a typical HER reaction under an acidic medium comprises two possible elementary reaction routes, Volmer-Heyrovsky and Volmer-Tafel (Fig. S12). The rate-determining step of HER mechanism is generally indicated by Tafel plot analysis, which is associated with the binding energy between the metal catalyst surface and hydrogen atoms [24,25]. From Fig. 4 (d), the Tafel slope of 20 wt % Pt is 35 mV dec<sup>-1</sup> which is corresponding to a Tafel limiting mechanism, whereas the TM-<sup>s</sup>MoS<sub>2</sub> and <sup>s</sup>MoS<sub>2</sub> are more likely to adopt a Volmer limiting mechanism in LSV measurement.

While testing the catalytic performance in the PEM electrolyzer, the fully acidified Nafion membrane (~0.1 S cm<sup>-1</sup>) is much more acidic than the 0.5 M H<sub>2</sub>SO<sub>4</sub> electrolyte [26]. The catalyst surface is readily covered with adsorbed hydrogen at a significant quantity in a local polarized acidic environment in PEM conditions, which eventually leads to a change of the rate-determining step to surface-H bond breaking. The reaction pathway is associated with the H recombination from surface-H in Tafel step; thus, the weaker surface-H bond of TMs allows surface migration and facilitates H<sub>2</sub> formation. Density functional theory calculations from Ferrin et al. [27] shows the surface-H binding energy as follows, Fe > Ni > Co > Cu, which matches the current density of PEM electrolyzer testing in general. However, Cu with the lowest binding energy giving the lower current density than Co and Ni is due to the structural distortion as mentioned in Fig. 5(d).

#### 4. Conclusions

In conclusion, we have provided direct visualization and experimental evidence that TM species can be atomically bonded to

the surface S sites of the basal plane of the monolayer MoS<sub>2</sub>. Meanwhile, we have also shown that the TM-MoS<sub>2</sub> can be applied in water splitting reactions in a real electrolyzer with industrial applicable conditions. HAADF-STEM imaging and XAS analysis clearly suggest that most TMs are in an oxidized form and that they are attached to the Mo atop sites of the basal plane. A trend for electrochemical performance in the electrolyzer has been established. The tetrahedral anchored Co in the absence of Co-Mo bond has induced the appropriate downshift of the conduction band such that highest HER activity can mainly occur at the S sites, which has granted Co-<sup>s</sup>MoS<sub>2</sub> the highest electrochemical activity. In contrast, the descending TM nuclear charge across the period from Fe to Cu has a direct influence on the TM-Mo bond strength which causes the overall deviation of ΔG<sub>H</sub> from zero. It is believed that TM-<sup>s</sup>MoS<sub>2</sub> could be used as an affordable alternative to the expensive Pt/C in electrolyzer.

#### Funding

We acknowledge the financial support from EPSRC-IUK (EP/N510026/1) and Siemens AG for this work.

#### Declaration of Competing Interest

The authors declare that they have no known competing financial interests or personal relationships that could have appeared to influence the work reported in this article.

#### Acknowledgements

The authors wish to thank the National Synchrotron Radiation Center, Hsinchu, Taiwan, for accessing EXAFS facilities. R.K. and K.S. acknowledge the JSPS KAKENHI (JP16H06333) for support.

#### Appendix A. Supplementary data

Supplementary data to this article can be found online at <https://doi.org/10.1016/j.mtadv.2019.100020>.



## References

- [1] B. Le Quéré, R.M. C. Andrew, P. Friedlingstein, S. Sitch, J. Hauck, J. Pongratz, P.A. Pickers, J.I. Korsbakken, G.P. Peters, J.G. Canadell, A. Arneeth, V.K. Arora, L. Barbero, A. Bastos, L. Bopp, F. Chevallier, L.P. Chini, P., D. Ciais, Supplemental data of global carbon budget 2018, *Glob. Carbon Proj.* 4 (2018) 2141–2194, <https://doi.org/10.18160/gcp-2018>.
- [2] S. Chu, A. Majumdar, Opportunities and challenges for a sustainable energy future, *Nature* 488 (2012) 294–303, <https://doi.org/10.1038/nature11475>.
- [3] L.C. King, J.C.J.M. Van Den Bergh, Implications of net energy-return-on-investment for a low-carbon energy transition, *Nat. Energy* 3 (2018) 334–340, <https://doi.org/10.1038/s41560-018-0116-1>.
- [4] I. Dincer, Green methods for hydrogen production, *Int. J. Hydrogen Energy* 37 (2012) 1954–1971, <https://doi.org/10.1016/j.ijhydene.2011.03.173>.
- [5] M. Carmo, D.L. Fritz, A comprehensive review on PEM water electrolysis, *Int. J. Hydrogen Energy* 38 (2013) 4901–4934, <https://doi.org/10.1016/j.ijhydene.2013.01.151>.
- [6] M.G. Walter, E.L. Warren, J.R. McKone, S.W. Boettcher, Q. Mi, E.A. Santori, N.S. Lewis, Solar water splitting cells, *Chem. Rev.* 110 (2010) 6446–6473, <https://doi.org/10.1021/cr1002326>.
- [7] B. Rausch, M.D. Symes, G. Chisholm, L. Cronin, Decoupled catalytic hydrogen evolution from a molecular metal oxide redox mediator in water splitting, *Science* 345 (2014) 1326–1330, <https://doi.org/10.1126/science.1257443>.
- [8] M. Li, K. Duanmu, C. Wan, T. Cheng, L. Zhang, S. Dai, W. Chen, Z. Zhao, P. Li, H. Fei, Y. Zhu, R. Yu, J. Luo, K. Zang, Z. Lin, M. Ding, J. Huang, H. Sun, J. Guo, X. Pan, W.A. Goddard, P. Sautet, Y. Huang, X. Duan, Single-atom tailoring of platinum nanocatalysts for high-performance multifunctional electrocatalysis, *Nat. Catal.* 2 (2019) 495–503, <https://doi.org/10.1038/s41929-019-0279-6>.
- [9] H. Hwang, H. Kim, J. Cho, MoS<sub>2</sub> nanoplates consisting of disordered graphene-like layers for high rate lithium battery anode materials, *Nano Lett.* 11 (2011) 4826–4830, <https://doi.org/10.1021/nl202675f>.
- [10] J. Xiao, D. Choi, L. Cosimbescu, P. Koech, J. Liu, J.P. Lemmon, Exfoliated MoS<sub>2</sub> nanocomposite as an anode material for lithium ion batteries, *Chem. Mater.* 22 (2010) 4522–4524, <https://doi.org/10.1021/cm101254j>.
- [11] Y. Li, H. Wang, L. Xie, Y. Liang, G. Hong, H. Dai, MoS<sub>2</sub> nanoparticles grown on graphene: an advanced catalyst for the hydrogen evolution reaction, *J. Am. Chem. Soc.* 133 (2011) 7296–7299, <https://doi.org/10.1021/ja201269b>.
- [12] A.B. Laursen, S. Kegnæs, S. Dahl, I. Chorkendorff, Molybdenum sulfides - efficient and viable materials for electro- and photoelectrocatalytic hydrogen evolution, *Energy Environ. Sci.* 5 (2012) 5577–5591, <https://doi.org/10.1039/c2ee02618j>.
- [13] K.S. Liang, R.R. Chianelli, F.Z. Chien, S.C. Moss, Structure of poorly crystalline MoS<sub>2</sub>-A modeling study, *J. Non-Cryst. Solids* 79 (1986) 251–273, [https://doi.org/10.1016/0022-3093\(86\)90226-7](https://doi.org/10.1016/0022-3093(86)90226-7).
- [14] E. Parzinger, E. Mitterreiter, M. Stelzer, F. Kreupl, J.W. Ager, A.W. Holleitner, U. Wurstbauer, Hydrogen evolution activity of individual mono-, bi-, and few-layer MoS<sub>2</sub> towards photocatalysis, *Appl. Mater. Today* 8 (2017) 132–140, <https://doi.org/10.1016/j.apmt.2017.04.007>.
- [15] Y. Yu, S.Y. Huang, Y. Li, S.N. Steinmann, W. Yang, L. Cao, Layer-dependent electrocatalysis of MoS<sub>2</sub> for hydrogen evolution, *Nano Lett.* 14 (2014) 553–558, <https://doi.org/10.1021/nl403620g>.
- [16] T.F. Jaramillo, K.P. Jørgensen, J. Bonde, J.H. Nielsen, S. Hørch, I. Chorkendorff, Identification of active edge sites for electrochemical H<sub>2</sub> evolution from MoS<sub>2</sub> nanocatalysts, *Science* 317 (2007) 100–102, <https://doi.org/10.1126/science.1141483>.
- [17] H. Tang, S. Roy Morrison, Optimization of the anisotropy of composite MoS<sub>2</sub> films, *Thin Solid Films* 227 (1993) 90–94, [https://doi.org/10.1016/0040-6090\(93\)90190-Z](https://doi.org/10.1016/0040-6090(93)90190-Z).
- [18] Z. He, W. Que, Molybdenum disulfide nanomaterials: structures, properties, synthesis and recent progress on hydrogen evolution reaction, *Appl. Mater. Today* 3 (2016) 23–56, <https://doi.org/10.1016/j.apmt.2016.02.001>.
- [19] T.H.M. Lau, X. Lu, J. Kulhavy, S. Wu, L. Lu, T.S. Wu, R. Kato, J.S. Foord, Y.L. Soo, K. Suenaga, S.C.E. Tsang, Transition metal atom doping of the basal plane of MoS<sub>2</sub> monolayer nanosheets for electrochemical hydrogen evolution, *Chem. Sci.* 9 (2018) 4769–4776, <https://doi.org/10.1039/c8sc01114a>.
- [20] G. Liu, A.W. Robertson, M.M.J. Li, W.C.H. Kuo, M.T. Darby, M.H. Muhieddine, Y.C. Lin, K. Suenaga, M. Stamatakis, J.H. Warner, S.C.E. Tsang, MoS<sub>2</sub> monolayer catalyst doped with isolated Co atoms for the hydrodeoxygenation reaction, *Nat. Chem.* 9 (2017) 810–816, <https://doi.org/10.1038/NCHEM.2740>.
- [21] J. Kibsgaard, A. Tuxen, K.G. Knudsen, M. Brorson, H. Topsøe, E. Lægsgaard, J.V. Lauritsen, F. Besenbacher, Comparative atomic-scale analysis of promotional effects by late 3d-transition metals in MoS<sub>2</sub> hydrotreating catalysts, *J. Catal.* 272 (2010) 195–203, <https://doi.org/10.1016/j.jcat.2010.03.018>.
- [22] J. Mo, B.I. Stefanov, T.H.M. Lau, T. Chen, S. Wu, Z. Wang, X.Q. Gong, I. Wilkinson, G. Schmid, S.C.E. Tsang, Superior performance of Ag over Pt for hydrogen evolution reaction in water electrolysis under high overpotentials, *ACS Appl. Energy Mater.* 2 (2019) 1221–1228, <https://doi.org/10.1021/acsaem.8b01777>.
- [23] H. Wang, C. Tsai, D. Kong, K. Chan, F. Abild-Pedersen, J.K. Nørskov, Y. Cui, Transition-metal doped edge sites in vertically aligned MoS<sub>2</sub> catalysts for enhanced hydrogen evolution, *Nano Res* 8 (2015) 566–575, <https://doi.org/10.1007/s12274-014-0677-7>.
- [24] J.K. Nørskov, T. Bligaard, J. Rossmeisl, C.H. Christensen, Towards the computational design of solid catalysts, *Nat. Chem.* 1 (2009) 37–46, <https://doi.org/10.1038/nchem.121>.
- [25] E. Skúlason, V. Tripkovic, M.E. Björketun, S. Gudmundsdóttir, G. Karlberg, J. Rossmeisl, T. Bligaard, H. Jonsson, J.K. Nørskov, Modeling the electrochemical hydrogen oxidation and evolution reactions on the basis of density functional theory calculations, *J. Phys. Chem. C* 114 (2010) 18182–18197, <https://doi.org/10.1021/jp1048887>.
- [26] L. Liu, W. Chen, Y. Li, An overview of the proton conductivity of nafion membranes through a statistical analysis, *J. Membr. Sci.* 504 (2016) 1–9, <https://doi.org/10.1016/j.memsci.2015.12.065>.
- [27] P. Ferrin, S. Kandoi, A.U. Nilekar, M. Mavrikakis, Hydrogen adsorption, absorption and diffusion on and in transition metal surfaces: a DFT study, *Surf. Sci.* 606 (2012) 679–689, <https://doi.org/10.1016/j.susc.2011.12.017>.